MaGSoundDST-3D automatic inversion of magnetic and gravity data based on the differential similarity transform

GEOPHYSICS, VOL. 75, NO. 1 (JANUARY-FEBRUARY 2010); P. L25–L38, 9 FIGS., 2 TABLES.
10.1190/1.3298619

MaGSoundDST — 3D automatic inversion of magnetic and gravity data based on the differential similarity transform

Daniela Gerovska[1], Marcos J. Araúzo-Bravo[2], Petar Stavrev[3], and Kathryn Whaler[1]

ABSTRACT

We present an automatic procedure — Magnetic And Gravity SOUNDing Differential Similarity Transform (MaGSoundDST) — for inversion of regular or irregular magnetic- and gravity-grid data measured on even or uneven surfaces. It solves for horizontal position, depth, and structural index of simple sources and is independent of a linear background. In addition, it estimates the shape of sources consisting of several singular points and lines. The method uses the property of the differential similarity transform (DST) of a magnetic or a gravity anomaly to become zero or linear at all observation points when the central point of similarity of the transform, which we refer to as the probing point, coincides with a source's singular point. It uses a measured anomalous field and its calculated or measured (gradiometry) first-order derivatives. The method is independent of the magnetization-vector direction in the magnetic data case and does not require reduction-to-the-pole transformed data as input. With MaGSoundDST, we provide an important alternative interpretation technique to the Euler deconvolution procedures, combining a moving-window method, whereby the solutions are linked to singular points of causative bodies, with an approach in which the solutions are linked to the real sources. The procedure involves calculating a 3D function that evaluates the linearity of the DST for different integer or noninteger structural indices, using a moving window. We sound the subsurface along a vertical line under each window center. Then we combine the 3D results for different structural indices and present them in three easy-to-interpret maps, avoiding the need for clustering techniques. We deduce only one solution for location and type of simple sources, which is a major advantage over Euler deconvolution. Application to different cases of synthetic and real data shows the method's applicability to various types of magnetic and gravity field investigations.

INTRODUCTION

The number of semiautomatic and automatic methods for inversion of potential fields is growing fast (Nabighian et al., 2005). Several methods are based on the homogeneity property of the potential fields from simple sources and use Euler's equation (Thompson, 1982; Reid et al., 1990; Stavrev, 1997; Hsu, 2002; Keating and Pilkington, 2004; Gerovska et al., 2005) or the direct expression of homogeneity (Moreau et al., 1997; Stavrev et al., 2006; Fedi, 2007). Another popular approach is to use the analytical expressions of different elements of the fields of certain geologic models, their transformations, and ratios (Hartman et al., 1971; Naudy, 1971; Hansen and Simmonds, 1993; Thurston and Smith, 1997; Stavrev, 2006).

The different techniques input derivatives of different orders of the magnetic or gravity potential or transformations that include them. Increasing derivative order makes the procedures more sensitive to noise in the data. Some of the methods take into account constant (Thompson, 1982; Hsu, 2002; Gerovska et al., 2005), linear (Stavrev, 1997; Gerovska and Araúzo-Bravo, 2003; Stavrev, 2006), or nonlinear (Dewangan et al., 2007) backgrounds. The homogeneity-based methods contend with the problem of relating the estimations of degree of homogeneity and location of detected singular points to real shapes. On the other hand, methods that assume a single source lack source resolution. Euler deconvolution procedures produce numerous dispersed solutions related to a single source, which makes them impractical without applying clustering tech-

Manuscript received by the Editor 3 April 2009; revised manuscript received 21 July 2009; published online 5 March 2010.
[1]University of Edinburgh, School of GeoSciences, Edinburgh, U. K. E-mail: dgerovsk@staffmail.ed.ac.uk; kathy.whaler@ed.ac.uk.
[2]Max Planck Institute for Molecular Biomedicine, Münster, Germany. E-mail: marcos.arauzo@mpi-mail.mpg.de.
[3]University of Mining and Geology St. Ivan Rilski, Department of Applied Geophysics, Sofia, Bulgaria. E-mail: pstavrev@mail.bg.

niques (Gerovska and Araúzo-Bravo, 2003; Mikhailov et al., 2003; Ugalde and Morris, 2008).

Our aim is to present a new automatic method to interpret potential-field data that produces a single solution corresponding to a simple source and links the methods using simple sources (e.g., Thompson, 1982; Reid et al., 1990) with those assuming real shapes (Thurston and Smith, 1997; Stavrev, 2006). The Magnetic And Gravity SOUNDing Differential Similarity Transform (MaGSoundDST) is based theoretically on the differential similarity transform (DST) (Stavrev, 1997; Stavrev et al., 2009). It accounts for a linear background in the data and uses as input the field and only its first-order derivatives, measured from gradiometry or calculated. The procedure sounds the space under the data along vertical lines for a set of structural-index values to produce a DST estimator-of-linearity field. Depending on its value, we determine whether, at a certain location, there is a gravity or a magnetic field source present and its type. Therefore, although we do not directly estimate magnetization or density as a function of depth as in well logging (Sheriff, 2002), we do undertake a kind of sounding — hence, the name of the method.

Afterward, three maps are compiled from the 3D estimator-of-linearity functions obtained for different structural indices. The anomalies of one map show the horizontal shape of the real sources, and its local minima indicate the horizontal positions of the simple sources. The other two maps show the structural-index distribution and the depth to the simple sources, respectively, based on the horizontal position of the local minima of the first map. The introduction of these three new maps helps obtain a single solution for each source detected, which is a significant step forward compared to procedures producing several spray solutions, sometimes referred to as strings of pearls.

METHOD

Theory

The potential fields used in applied geophysics are space phenomena that can be described in terms of affine geometry. In a 3D affine space, the transform of similarity is a linear transformation of coordinates using the equations (e.g., Gellert et al., 1979)

$$x' = tx + (1-t)a, \quad y' = ty + (1-t)b,$$

$$z' = tz + (1-t)c, \tag{1}$$

where t is a coefficient of similarity, (a,b,c) are the coordinates of a central point of similarity (CPS), and $P'(x',y',z')$ is the similar image of the original point $P(x,y,z)$. If $t \geq 1$, then the geometric objects preserve their integrity, shape, and orientation but change their sizes by the coefficient t^d, where d is the space dimension of the geometric object and $d = 0$, 1, 2, or 3. Operator 1 for $t > 0$ shifts the observation points and the sources of a potential field, thus affecting the field values in the transformed space. The difference between the original and the transformed fields provides information about the source parameters (Stavrev, 1997).

The similarity transformed field A' of an anomaly A can be calculated using the expression

$$A'(x',y',z') = t^n A(x,y,z), \tag{2}$$

where n is the degree of extended homogeneity of the gravity or magnetic anomaly A with respect to all quantities of length dimension in the analytical expression of A (Stavrev and Reid, 2007). The degree of homogeneity is $n = d - s - k$, where s is an index for the type of gravity and magnetic sources to be used (1 for point masses and equivalent poles, 2 for dipoles, 3 for equivalent quadrupoles) and where k characterizes A as a derivative of the potential of certain order $k = 0, 1, 2, 3, \ldots$.

The normalized finite-difference similarity transform (FDST) for A is defined as

$$D(x',y',z') = \frac{A'(x',y',z') - A(x',y',z')}{t-1}, \tag{3}$$

where $A'(x',y',z')$ is given by equation 2 and $A(x',y',z')$ can be measured at level z' or calculated through analytical continuation of $A(x,y,z)$.

The DST is the limit of the FDST when the coefficient t in equation 3 tends to one (see Appendix A). The result is the analytical expression $S_A(x,y,z)$ of the DST (Stavrev, 1997):

$$S_A(x,y,z) = nA + (a-x)\frac{\partial A}{\partial x} + (b-y)\frac{\partial A}{\partial y} + (c-z)\frac{\partial A}{\partial z}, \tag{4}$$

where A, its gradient components $\partial A/\partial x = A_x$, $\partial A/\partial y = A_y$, and $\partial A/\partial z = A_z$, its degree of homogeneity n, and the components $(a-x)$, $(b-y)$, $(c-z)$ of the distance vector $\mathbf{r}_{PC}$ from the observation point $P(x,y,z)$ to the CPS $C(a,b,c)$ are related linearly. The CPS position and the degree n are parameters of the DST function $S_A(x,y,z)$.

The DST function $S_A(x,y,z)$ can be treated as an anomalous field related to A (Stavrev, 1997). For example, the gravity potential $V(x,y,z)$ of a point mass m at point $M(x_0,y_0,z_0)$ with degree of homogeneity $n = -1$ generates a DST function (see Appendix B)

$$S_V(x,y,z) = -V(x,y,z) + \mathbf{r}_{PC}\cdot\nabla_P V = Gm\mathbf{r}_{CM}\cdot\nabla_M \frac{1}{r_{MP}}, \tag{5}$$

where G is the gravitational constant and $\mathbf{r}_{CM}$ is the vector pointing from C to M. The right-hand side of expression 5 is analogous to the expression for the potential of a point magnetic dipole. Thus, the DST of V is an anomaly of equivalent "gravity" dipole with a moment $Gm\mathbf{r}_{CM}$ proportional to the distance vector $\mathbf{r}_{CM}$. In the case of a magnetic anomaly of a dipole at point M, the equivalent source of the DST is a magnetic quadrupole at M with a moment depending on $\mathbf{r}_{CM}$ (Stavrev, 1997).

The examples above show the physical sense of the DST from anomalies of point sources. As a point C approaches the point source at M, the moment of the equivalent source decreases; hence, the amplitude of the DST S also decreases. If C and M coincide, $r_{CM} = 0$ and the DST $S = 0$ for all observation points $P(x,y,z)$. Thus, using a

moving CPS as a probing point, we can locate the singular point M and recognize its type through the parameter n.

The same possibility for a field inversion is valid for all other types of singular points at $M(x_0,y_0,z_0)$ of gravity and magnetic anomalies (Stavrev, 1997). This common property can be proved by substituting (a,b,c) with (x_0,y_0,z_0) in equation 4:

$$S_A(x,y,z) = nA + (x_0 - x)\frac{\partial A}{\partial x} + (y_0 - y)\frac{\partial A}{\partial y} + (z_0 - z)\frac{\partial A}{\partial z} = 0,$$

which is an equivalent form of Euler's well-known differential equation for one-point sources (e.g., Reid et al., 1990). In this particular case, the DST approach results in a solution $x_0 = a$, $y_0 = b$, $z_0 = c$ of Euler's equation for an isolated field A with one singular point.

The DST of potential fields of sources with complex shape and distribution of physical properties has its respective integral expressions and physical sense (Stavrev, 1997). The value S_A is a continuous function that decreases as the CPS approaches the field's singular point. This allows the design of effective deconvolution techniques, including those suitable for more than one singular point (Stavrev, 1997; Stavrev et al., 2009).

The DST approach can be used in automatic deconvolution techniques in the presence of a constant or linear background. The observed field — say, F — usually contains a local anomaly A and a background B, i.e., $F = A + B$. Within A, the background B can be considered as a constant or a linear field $B(x,y,z) = l + ux + vy + wz$. Then, operator 4 applied to F results in

$$\begin{aligned} S_F(x,y,z) &= n(A + B) + (a - x)\frac{\partial(A + B)}{\partial x} \\ &\quad + (b - y)\frac{\partial(A + B)}{\partial y} + (c - z)\frac{\partial(A + B)}{\partial z} \\ &= S_A(x,y,z) + (nB + (a - x)u + (b - y)v \\ &\quad + (c - z)w) = S_A(x,y,z) + S_B(x,y,z), \end{aligned} \tag{6}$$

where $S_B(x,y,z)$ is a linear function of the coordinates of the observation points.

If a CPS $C(a,b,c)$ coincides with the singular point $M(x_0,y_0,z_0)$ of anomaly A, then $S_A(x,y,z) \equiv 0$, and $S_F(x,y,z)$ takes the form of a plane surface $S_B(x,y,z)$. Thus, the inversion of A in the presence of a linear background B can be implemented by a search for the position of the CPS and the degree n that make the DST of F linear.

In an inverse procedure, the deviations of the data from the assumed interpretation model can be considered as systematic noise. The observed field F also contains random noise. If the sum of these two types of noise is denoted by $O(x,y,z)$, then $F = A + B + O$. The DST operator 4 is a linear operator; hence,

$$S_F(x,y,z) = S_A(x,y,z) + S_B(x,y,z) + S_O(x,y,z) \tag{7}$$

for the accepted degree of homogeneity of the target anomaly A.

The MaGSoundDST inversion procedure is a 3D Euler deconvolution based on the property of the DST considered above. The pattern of DST for different CPS from 2D interpretation models in wide use is detailed in Stavrev et al. (2009).

Estimating the linearity of the DST function

The linearity of a DST surface S through the observation points within a window W is estimated by the residual dispersion after linear regression:

$$q_S^2(a,b,c;n) = (j - 1)D_S^2(1 - K^2), \tag{8}$$

where j is the number of observation points, D_S^2 is the dispersion, and K is the generalization of the correlation coefficient of S to the 3D case,

$$K = \frac{1}{(j - 1)D_S D_x D_y}\sum_{i=1}^{j}(S_i - S_{\text{ave}})(x_i - x_{\text{ave}})(y_i - y_{\text{ave}}),$$

$$D_S^2 = \frac{1}{j - 1}\sum_{i=1}^{j}(S_i - S_{\text{ave}})^2$$

where S_{ave}, x_{ave}, and y_{ave} are the average values of the S function and the x- and y-coordinates in the frame of W:

$$D_x^2 = \frac{1}{j - 1}\sum_{i=1}^{j}(x_i - x_{\text{ave}})^2 \text{ and } D_y^2 = \frac{1}{j - 1}\sum_{i=1}^{j}(y_i - y_{\text{ave}})^2.$$

The estimator q_s gives the minimal deviation of the DST function from its linear approximation, say, $L(x,y,z)$, in the frame of W. If a CPS coincides with the source's singular point, then the L and S_B linear functions also coincide. In other cases, L may deviate from S_B and the real background B cannot be estimated.

When $q_S = 0$ for a window W, $S_F(x,y,z)$ is a linear function of the horizontal coordinates. In the presence of noise, q_S has a nonzero minimum, reflecting the noise residual standard deviation q_δ. The estimator of linearity q_S can be normalized by the residual standard deviation q_F of the field F. Thus, the corresponding normalized relative standard deviation Q takes the form

$$Q(a,b,c;n) = \frac{q_S(a,b,c;n)}{q_F}, \tag{9}$$

where q_F is calculated using expression 8 for the function F instead of the function S. The minimum value of Q corresponds to the maximum linearity of the DST.

The normalized estimator Q attains small values when q_F has high values, i.e., around the extreme points of the anomalous field near the horizontal position of the source's singular point where at the same time q_S has small values because $S_A(x,y,z)$ is close to zero. The estimator Q increases when moving away from the singular point; where the value of q_s is high, the anomalous field intensity is small and the standard deviation q_F is also small. Thus, the distribution of the estimator Q takes into account the anomalous intensity and con-

figuration, and is used for selecting reliable results from the inverse procedure.

The negative of the degree of homogeneity n, $N = -n$, which is called the structural index (after Thompson, 1982), reflects the type of source geometry. It has attained popularity in practice; therefore, from here on, we use the term structural index instead of degree of homogeneity and the respective notation. A full description of the structural indices N of simple interpretation models is given in Stavrev and Reid (2007).

Implementing the inversion method

The MaGSoundDST algorithm involves calculating the function $Q(a,b,c)$ of the field in the space under the surface of observations for a series of assumed structural indices N using a moving window W along the observation surface. It is a technique for processing data sets comprising many, rather than one or two isolated, anomalies, so we looked for a more compact and easy way to compare numerous subsets of 3D functions. Thus, first we introduced a new 2D map $Q(Q_{\min})$ that combines all subsets of 3D functions $Q(a,b,c;N)$ into a bidimensional one by obtaining a single $Q_{\min}$ value for each vertical probing line at each (a,b) horizontal location (see Figure 1a). The horizontal positions of the local minima of the so-obtained $Q(Q_{\min})$ map determine the horizontal positions of simple sources.

The values of the structural index N and the CPS depth c corresponding to each local minimum of the $Q(Q_{\min})$ map give the structural index and depth, respectively, of the corresponding simple sources (Figure 1a); these are mapped as $N(Q_{\min})$ and $Z(Q_{\min})$, respectively. The three new maps $[Q(Q_{\min}), N(Q_{\min}),$ and $Z(Q_{\min})]$ help to estimate and present in a compact way not only the location and structural index of simple sources, but also the shape of more complex sources composed of several singular points and lines.

MaGSoundDST is implemented in a nine-step process. First, we choose the CPS grid spacing and the number of probe points along the vertical line under each window center (a,b) to cover the expected depths of the sources (see Figure 1a).

Second, we choose the moving-window size. To detect the sources, the dimensions of the window should be at least twice the anticipated depth to the sources. Several window sizes should be tried to find the optimal one, taking into account the main wavelength of the observed anomaly or set of anomalies.

Third, we calculate the estimator of linearity $Q(a,b,c;N)$ for a set of structural indices between 0 and 3 for magnetic anomalies and -1 and 2 for gravity anomalies (where negative values are appropriate for gravity anomalies of transition type from thick contact models) using equations 9, 8, and 4. The structural indices may have integer or noninteger values to achieve higher resolution in the estimates. The larger the number of the structural indices tested, the higher the resolution. We introduce a 4D representation of $Q(a,b,c;N)$ based on a color codification of the values of Q in a 3D space (see, e.g., Figure 2c-f in the following section).

Fourth, we calculate a $Q(Q_{\min})$ map by finding the minimum value of $Q(a,b,c;N)$ at each horizontal position (a,b) for all structural indices N and all depths c, i.e., the $Q(Q_{\min})$ map is a map of $Q_{\min} = Q_{\min}(a,b) = \min_{c,N} Q(a,b,c;N)$ (see Figure 1a and Figure 2b).

Fifth, we find the local minima $(Q(Q_{\min}))_{\min}$ of the $Q(Q_{\min})$ map, for example, marked with a red circle in Figure 2b. A $(Q(Q_{\min}))_{\min}$ is accepted if it is less than one, when the residual standard deviation q_s of the DST is smaller than the residual standard deviation q_F of the original field, because the DST should be straighter than the original anomaly. This acceptance threshold value could be set lower for precise estimates, or it could be set higher, depending on the existing signal-to-noise ratio (S/N). The minima of the $Q(Q_{\min})$ map determine the horizontal positions of singular points of the complex sources. The pattern of the anomalies of the $Q(Q_{\min})$ map define the shape of the horizontal projections of complex sources such as intrusive sills, effusive plates, and horizontal rods.

Sixth, we calculate an $N(Q_{\min})$ map by finding the structural index corresponding to each value of the $Q(Q_{\min})$ map. The values of the $N(Q_{\min})$ map at horizontal positions of the local minima of the $Q(Q_{\min})$ map determine structural indices of singular points. The specific terraced pattern of the $N(Q_{\min})$ maps also helps to determine the shape of the horizontal projection of the sources.

Seventh, we calculate a $Z(Q_{\min})$ map by finding the CPS depth corresponding to each Q value from the $Q(Q_{\min})$ map. The $Z(Q_{\min})$ values corresponding to the local minima in the $Q(Q_{\min})$ map provide estimates of the depths to the singular points, defined by these minima.

Eighth, we improve the locations of the minima of the $Q(Q_{\min})$ map so their respective simple sources are not restricted to CPS grid points. The accuracy of MaGSoundDST in determining the coordinates of simple sources is not limited by the spacing of the window points and by the spacing of the vertical probe points. Once we find the minima of the $Q(Q_{\min})$ map, the grid position of the singular point corresponding to each minimum of $Q(Q_{\min})$, $(Q(Q_{\min}))_{\min}$, is refined. For each $(Q(Q_{\min}))_{\min}$, the MaGSoundDST procedure goes back to the original location of the $Q_{\min}$ value in the 3D function $Q(N)$, from which $Q_{\min}$ was extracted according to the rule described in step 4 (red sphere in Figure 1a). In the one-sphere case in Figure 2, this is the grid point with coordinates (5,5,1) km from $Q(N = 3)$. Then, from the Q values of all one-grid-point-radius nearest neighbors (see Figure 1b), interpolate the best-fitting ellipsoid of constant Q value; its center is the refined singular point location. The CPS grid points involved in implementing this refinement form a truncated cube, i.e., without the eight vertices (cuboctahedron), shown in green in Figure 1b. When we apply the refinement procedure, we find local minima at any point, as opposed to the discrete minima confined to the CPS grid positions. The coordinates of these new refined Q minima are the estimated locations of the simple sources.

Finally, if necessary, we eliminate automatically those minima of $Q(Q_{\min})$ that coincide with points of the (a,b) probing set where the windows are in the periphery of the anomalous fields, far from the targeted singular points, where the field gradient is low. For small windows, they also may fall on the flanks of an anomaly, where field behavior is close to linear. Deconvolution using data in such windows is unstable and the respective results are unreliable. Recognition of such points (a,b) is based on the value of q_F in the window W with center at the point (a,b). If q_F is less than an accepted after-test threshold $(q_F)_{\min}$, then the minimum of $Q(Q_{\min})$ at the respective point (a,b) should be rejected. We find a suitable $(q_F)_{\min}$ to be 75% of the maximum of q_F. Note that q_F is dependent on window size and field gradient.

RESULTS

Model tests

We applied MaGSoundDST to four different model data sets to demonstrate various features of the technique. The first example is

the inversion of the field of a magnetized sphere; it shows that MaGSoundDST works successfully on magnetic field data, is robust to random noise, and can correctly estimate source coordinates when the source does not coincide with a CPS grid point. The second example is the inversion of magnetic data from five sources with interfering fields; it demonstrates that the technique works in the presence of a linear background, that one solution is obtained per singular point, and that the three newly introduced maps help to relate the solutions for singular points to real sources. The third simple example, the inversion of the gravity field of a spherical mass, demonstrates that MaGSoundDST works well with gravity data from simple sources. The fourth example illustrates an application to gravity anomalies of transition type, i.e., from sources characterized by a noninteger negative structural index.

The first example is noise-free magnetic model data of 40×40 points, generated by a spherical source (Figure 2a) with center at $(x_0 = 5, y_0 = 5, z_0 = 1)$ km and having an induced magnetization with inclination of 45° and declination of 0°. The CPS (a,b,c) set has a 3D grid spacing of $0.25 \times 0.25 \times 0.25$ km. The moving window is 21×21 points (5×5 km). The lower half-space was probed with six points along a vertical line under each window center. The minimal Q_{min} obtained from the four tested structural indices (Figure 2c-f) is for $N = 3$ ($Q_{min} = 0.00$), which corresponds to a spherical source with center estimated at $(a = 5, b = 5, c = 1)$ km.

For $N = 0$ (Figure 2c) and $N = 1$ (Figure 2d), no local minima of Q were detected. Note that for inappropriate values of N, $Q(N)$ may not have any minima. A tentative value of $N = 2$ resulted in a Q_{min} of 0.44 for a CPS at $(a = 5, b = 5, c = 0.6)$ km. Figure 2b shows the newly introduced map $Q(Q_{min})$, which combines the four 3D maps $Q(N)$, namely, $Q(0)$, $Q(1)$, $Q(2)$, and $Q(3)$ as described in step 4 of the process and illustrated in Figure 1a, correctly estimating the source position.

To check the performance of the local minimum refinement, we tested the technique on the magnetic field caused by the same spherical source but located at $(x_0 = 4.85, y_0 = 5.15, z_0 = 0.85)$ km, i.e., the source does not coincide with a point of the CPS grid. If we use the discrete minima option, the estimated sphere location is $(a = 4.75, b = 5.25, c = 0.75)$ km for $(Q(Q_{min}))_{min} = 0.38$. If we use the option for refined minima (step 8), the refined location of the source is $(a = 4.85, b = 5.14, c = 0.85)$ km for $(Q(Q_{min}))_{min} = 0.38$, which is virtually coincident with the true source position.

Hypothesizing that each magnetic sensor for the signals A, A_x, A_y, and A_z could be affected by independent Gaussian noise, we performed a perturbation analysis. We contaminated the four input channels A, A_x, A_y, and A_z for the analytical spherical magnetic case with zero mean, Gaussian-distributed random noise in the range 10–15-dB S/N in 1-dB increments. We simulated 100 replicates for each S/N; the perturbations of $(Q(Q_{min}))_{min}$ and its respective parameters (a,b,c,N) determined by MaGSoundDST are plotted in Figure 3. MaGSoundDST is robust for S/N of 11 dB and higher. The maximum amplitude of the noise for S/N of 11 dB is about 40 nT (Figure 3), and the amplitude of the anomaly is about 300 nT (Figure 2a). For modern surveys, the noise level is less than 1 nT, which means

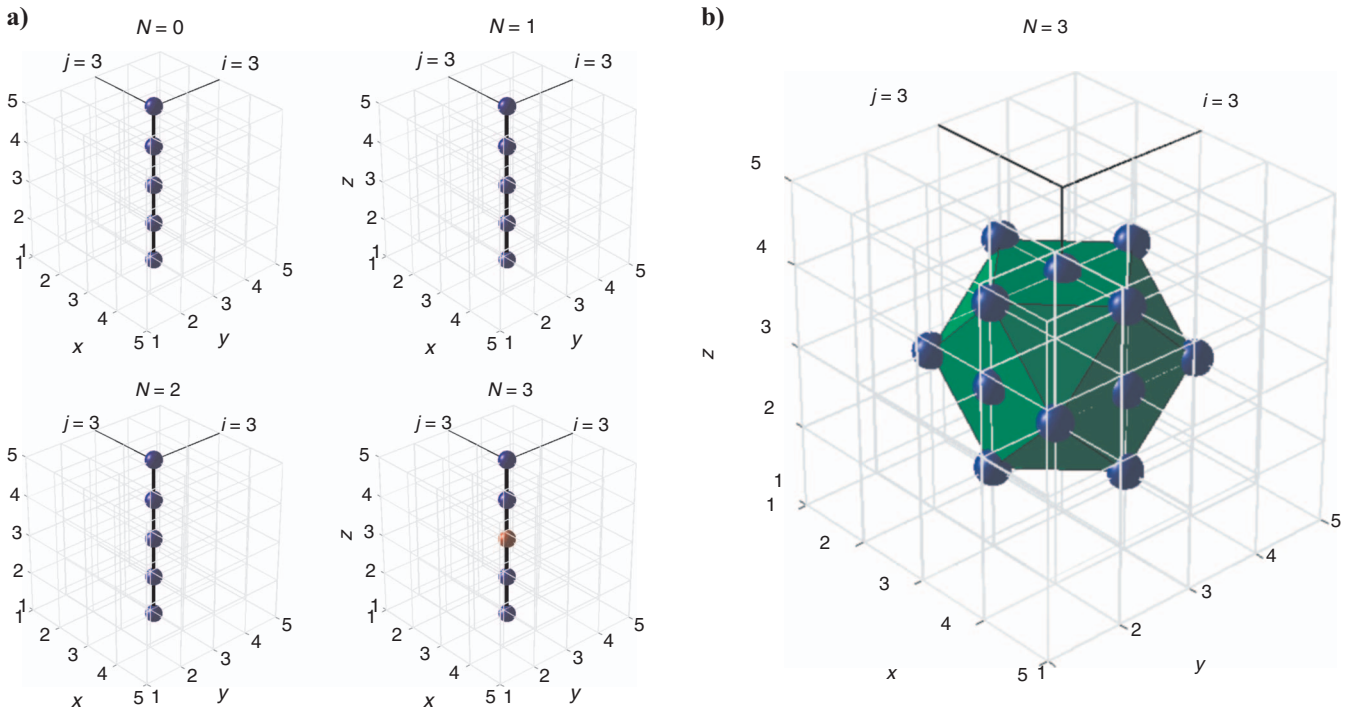

Figure 1. Method of implementation. (a) Vertical trace line of the sounding method across the 3D Q matrices associated with all tested structural indices. The blue spheres are the tentative probe points aligned on the vertical probing track line. The red sphere corresponds to the calculated local minimum grid point. The $Q(Q_{min})$ map takes at point (i,j) the Q at the red sphere location, $N(Q_{min})(i,j) = 3$, $Z(Q_{min})(i,j) = 3$ length units. (b) Set of grid points used to interpolate the local minimum around the calculated local minimum grid point. The interpolating grid points, shown with blue spheres, define a cuboctahedron, shown in green.

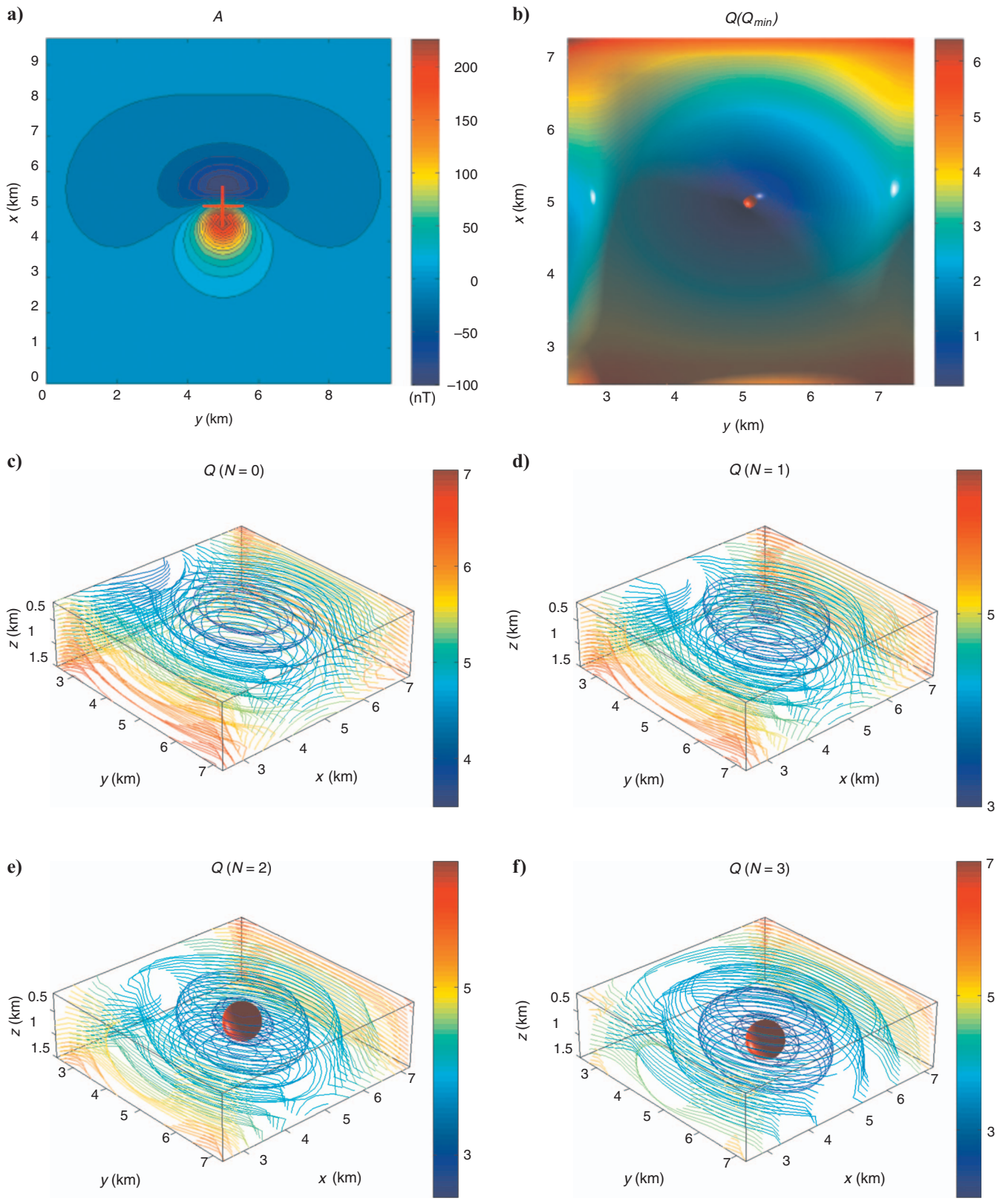

Figure 2. Model data set caused by a spherical magnetic source. (a) Anomalous magnetic field ΔT, in nT; (b) $Q(Q_{\min})$ with minimum correctly locating the source position; (c-f) 3D maps of the estimator $Q(a,b,c;N)$ of DST for structural indices $N = 0$, 1, 2, and 3. The red spheres denote the locations of local minima of Q and thus of the singular point (center) of the source. The view of the 3D contour maps Q has an azimuth of 48° and elevation of 30°.

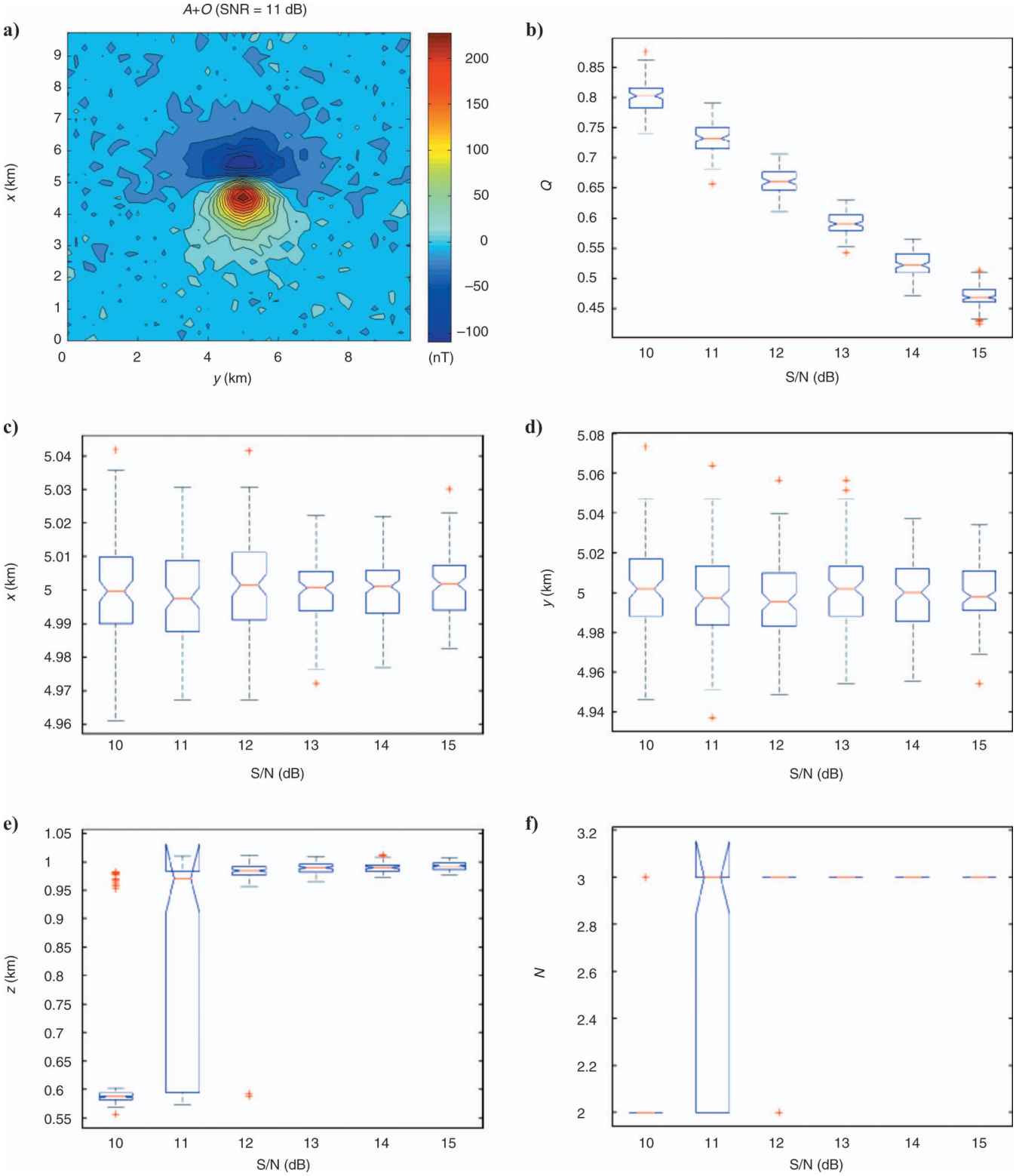

Figure 3. Noise analysis for the spherical-magnetic-source case. (a) Map of the corrupted signal A with one noise sample $O(\mathrm{S/N} = 11\ \mathrm{dB})$ and (b-f) box plots of the distribution of the variability of $(Q(Q_{\min}))_{\min}$ and its respective parameters a, b, c, N for different S/N-contaminated signals. The box associated with each S/N has horizontal lines at the lower quartile, median, and upper quartile values. Whiskers extend to the most extreme values within 1.5 times the interquartile range from the ends of the box, and outliers are displayed with a red plus sign. Notches display the variability of the median between samples. The width of a notch is computed so that box plots whose notches do not overlap have different medians at the 5% significance level. The significance level is based on a normal distribution assumption.

that MaGSoundDST should perform well on interpreting anomalies as small as 300/40 = 7.5 nT.

The second model example is the inversion of synthetic data generated by five magnetic bodies with individual fields, interfering somewhat to produce a linear or nonlinear background within certain windows. This is the same model used to test the Euler deconvolution method based on the DST by Gerovska and Araúzo-Bravo (2003). The five bodies are two spheres, a sill, a vertical dike and a horizontal rod, characterized by 10 singular points (Figure 4a and Table 1). The input data grid has 150 × 150 points. MaGSoundDST was applied for a CPS (a,b,c) set with a 3D grid spacing of 0.25 × 0.25 × 0.1 km, a window of 11 × 11 points (2.5 × 2.5 km), and 40 vertical probe points.

Figure 5 shows the 3D Q spaces for tentative integer values 0, 1, 2, and 3 of the structural index and the numerous local minima corresponding to each space. When we combine these four 3D spaces according to the procedure described in step 4 of the process, we obtain a 2D $Q(Q_{min})$ map with only 10 local minima. The three maps, $Q(Q_{min})$, $N(Q_{min})$, and $Z(Q_{min})$, are shown in Figure 4. The 10 local minima of $Q(Q_{min})$ estimate the horizontal positions of singular points. Two of the singular points of source S2 are not detected with minima of $Q(Q_{min})$ because of the proximity of the other two singular points, but this is compensated for by the fact that the overall horizontal shape of the source is given by the pattern of $Q(Q_{min})$. Source S3 (vertical dike) and the horizontal rod S4 are each detected by three minima.

The accuracy of the estimation is similar to that of the Euler deconvolution procedure based on the DST (Gerovska and Araúzo-Bravo, 2003). Furthermore, with the new procedure, we avoid the process of reducing the large number of spurious solutions to one estimate corresponding to each source and the necessary provision by the interpreter of parameters of closeness accompanying it. The maps $Q(Q_{min})$, $N(Q_{min})$, and $Z(Q_{min})$, over which the minima of $Q(Q_{min})$ are overlain, help to link the detected singular points and their estimated structural indices to fully shaped, real sources. This is a useful feature lacking in the representation of results by the standard Euler deconvolution procedure.

The third model example is a noise-free gravity data set caused by a spherical source (Figure 6) with center at ($x_0 = 60$, $y_0 = 60$, $z_0 = 9$) km, having a 5-km radius and a 1-g/cm^3 density contrast. The input data grid is 120 × 120 points. We applied MaGSoundDST with a window of 21 × 21 points (20 × 20 km). The CPS grid has a 3D grid spacing of 1 × 1 × 1 km and 15 vertical probe points. MaGSoundDST returns the correct horizontal position of (60, 60) km, depth of 9 km, and structural index of 2. The 3D maps of the estimator $Q(a,b,c;N)$ for structural indices $N = 0$, 1, and 2 are given in Figure 7.

The fourth example is gravity-field inversion of Keating's (1998) model of two adjacent prisms measuring 2 × 2 km and buried at a depth of 200 m. Both prisms have a depth extent of 5 km and are located 1 km apart. Their density contrast is 0.25 g/cm^3. The gravity grid has 100 × 200 points and 50-m spacing in the two directions. MaGSoundDST was applied with an 11 × 11 data window (500 × 500 m) and 60 vertical probe points. The CPS grid has a 3D grid spacing of 50 × 50 × 50 m. The results are shown in Figure 8. All of the estimates obtained indicate sources with structural indices of −0.5.

Keating (1998) uses a conventional Euler deconvolution with prescribed structural index of 0 and estimates a depth "of around 250 m." Stavrev and Reid (2007) show that for the gravity anomaly of a vertical contact model between depths of one and five relative units, considered as a one point source, the structural index N can vary from −0.1 to 0.5, being 0 for a thin sheet. For the gravity anomaly created by the same vertical contact model considered as a two-point source, they obtain N between −0.15 and −1.25, with $N = -1$ for a contact of considerable thickness. The thickness of our prisms is bigger than that in the study of Stavrev and Reid (2007) for a contact with substantial thickness, but the prisms deviate considerably from the model of a 2D contact. The depth estimates for the solutions are between 150 and 350 m, with a mean of 210 m and standard deviation of 7.54 m, for $Q(Q_{min})$ between 0.02 and 0.06 — closer to the true depth of 200 m than the "around 250 m" estimated by Keating (1998).

Magnetic data example from the Burgas region and adjoining Black Sea shelf, southeast Bulgaria

The anomalous magnetic field in the Burgas region of Bulgaria and the adjoining shelf is caused by the products of Upper Cretaceous magmatism, mainly by the Senonian andesite-basaltic and trachyandesite-trachybasaltic effusive formations and by the intrusive gabbro-monzonite-syenitic formation (Dachev, 1988). The structure of the anomalous magnetic field over the shelf indicates the orientation of regional faults as well as the location of large basic and ultrabasic bodies at depth, intruding along the faults. Northwest-southeast faults (135°) and, to some extent, east-west faults (90°–100°) manifest as magma-path structures. The geology and magnetic field of the region are described in more detail in Gerovska et al. (2009).

We applied MaGSoundDST on a total-field, 128 × 180-point magnetic data grid ΔT from southeast Bulgaria (Figure 9a), covering an area of the Burgas depression and the adjoining Black Sea shelf, using a CPS set with 3D grid spacing of 0.5 × 0.5 × 0.1 km and a window of 31 × 31 points (15 × 15 km). The lower half-space was probed up to a depth of 5 km (50 points). The inversion results are in Figure 9b-d and Table 2. We used a set of eight structural indices from −0.5 to 3 in increments of 0.5. We also used a threshold value of 2 (determined by trial and error) for Q because of the low S/N, to accommodate the high interference level and the deviation from anomalies from simple sources. If we compare the $Q(Q_{min})$ and $N(Q_{min})$ maps with the magnitude magnetic anomaly $T = (X^2 + Y^2 + Z^2)^{1/2}$ of the region by Stavrev and Gerovska (2000), the $Q(Q_{min})$ map and especially the terraced-pattern $N(Q_{min})$ map outline very well the shape of the horizontal projections of the complex sources.

We found 16 solutions (Table 2). Solution 9 corresponds to the most intense negative anomaly, located to the west of the city of Burgas. According to the comparison of the magnitude magnetic transforms T, E, and L by Stavrev and Gerovska (2000), which are transforms of different order of the magnetic potential, the source indicated by estimate 9 is deeper than the other sources in the area. The estimated structural index is 1, which suggests a sheet or dike source, and depth to the top of 1.9 km. Another group of estimates, 13–16, corresponds to the elongated west-northwest-east-southeast-trending anomaly to the east of Nesebar. The structural index for them is 1.5, which indicates a dike limited in depth. The depth to an

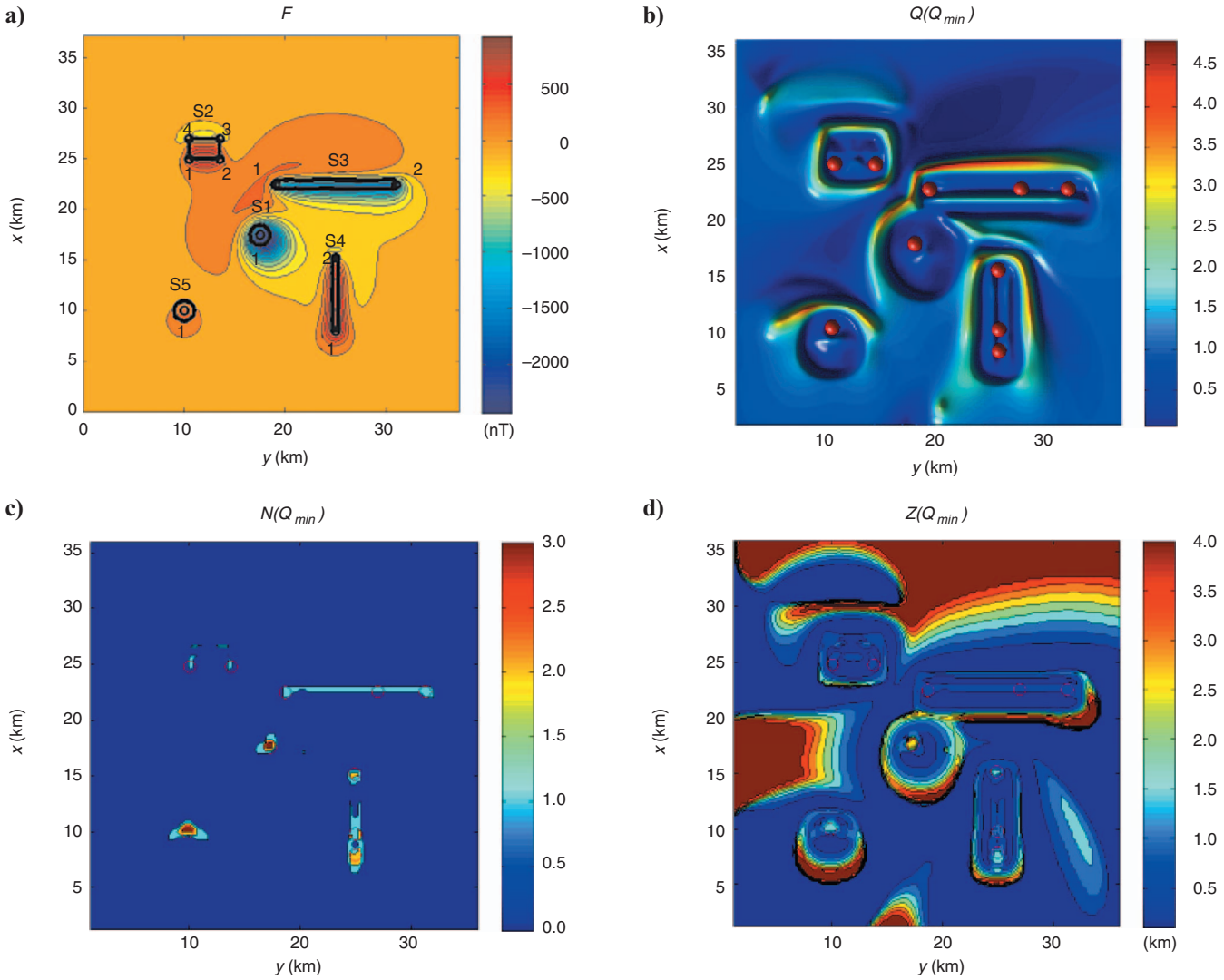

Figure 4. Model magnetic data set caused by five bodies: S1 and S5 (spheres), S2 (sill), S3 (vertical dike), and S4 (horizontal rod). (a) Anomalous magnetic field, in nT; (b) $Q(Q_{\min})$; (c) $N(Q_{\min})$; (d) $Z(Q_{\min})$ km.

Table 1. Real (x_0,y_0,z_0,N) and estimated (a,b,c,N_{est}) parameters of the singular points (SP) of the five bodies causing the magnetic anomalies in Figure 4a. The threshold value for Q is one.

Source	SP	x_0 km	a km	y_0 km	b km	z_0 km	c km	N	N_{est}	$(Q(Q_{\min}))_{\min}$
S1 sphere	1	17.5	17.6	17.5	17.4	3.0	3.0	3	3	0.07
S2 sill	1	25.0	24.8	10.5	10.2	1.0	0.9	1	1	0.47
	2	25.0	24.7	13.5	13.9	1.0	0.8	1	1	0.56
	3	27.0		13.5		1.0		1		
	4	27.0		10.5		1.0		1		
S3 dike	1	22.5	22.5	19.0	18.7	1.0	0.8	1	1	0.08
	2	22.5	22.5	31.0	31.3	1.0	0.8	1	1	0.07
			22.5		27.0		0.8		1	0.07
S4 horizontal rod	1	8.0	7.9	25.0	25.0	1.5	1.5	2	2	0.07
			9.8		25.0		1.0		1	0.21
	2	15.25	15.2	25.0	24.9	1.5	1.5	2	2	0.17
S5 sphere	1	10.0	10.0	10.0	9.9	2.0	1.9	3	3	0.15

internal point between the top and the center point of this subvertically extended body elongated west-northwest-east-southeast around 1.2 km (see Gerovska et al., 2005). For the same body, Stavrev (2006) obtains a structural index $N = 1.82$ and depth to the top of 1.5 km using magnitude transform ratios. Solution 5 in the Black Sea shelf is for a structural index of 1 (dike) and depth to the top of 1.3 km. The intense positive anomaly to the north of the town of Primorsko generated solution 2, having a structural index of 0.5 and depth of 1.2 km. The source of this anomaly, the Rossen intrusive (part of the Rossen ringlike palaeovolcanic center), outcrops in the coastal area. In this case, $N = 0.5$ can be interpreted conditionally because the minimum from the $Q(Q_{min})$ map does not coincide with the respective maximum area in the $N(Q_{min})$ map. The maximum area in the $N(Q_{min})$ map corresponding to estimate 2 has a value of around 1, appropriate for a dike. The depth of 1.2 km can be interpreted as a depth to an internal point of the dike because the dike outcrops. The results obtained with MaGSoundDST from this field example can be compared with results using Euler deconvolution based on the differential similarity transform (Gerovska and Araúzo-Bravo, 2003). The advantage of the simple presentation of the MaGSoundDST solutions over the Euler deconvolution results without clustering are worth noting. A good clustering technique, though, as proposed in Gerovska and Araúzo-Bravo (2003), can alleviate the problem of presentation of the results from Euler deconvolution.

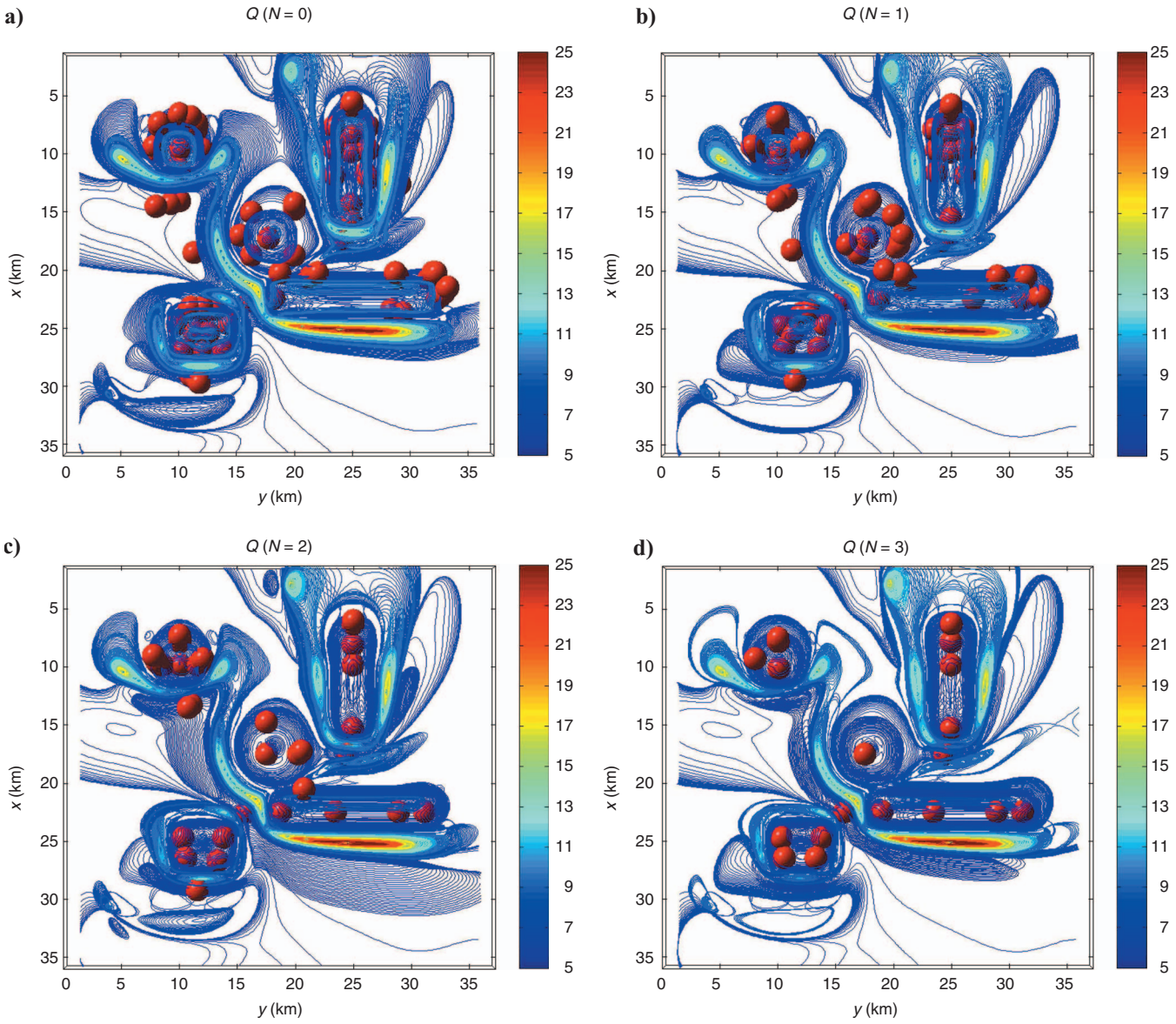

Figure 5. The 3D maps of the estimator $Q(a,b,c;N)$ of the DST for the five-body case for structural indices $N = 0$, 1, 2, and 3. The red spheres denote the location of local minima of $Q(a,b,c;N)$ and thus of singular points of the sources. The view of the 3D contour maps Q has an azimuth of zero and elevation of $-90°$.

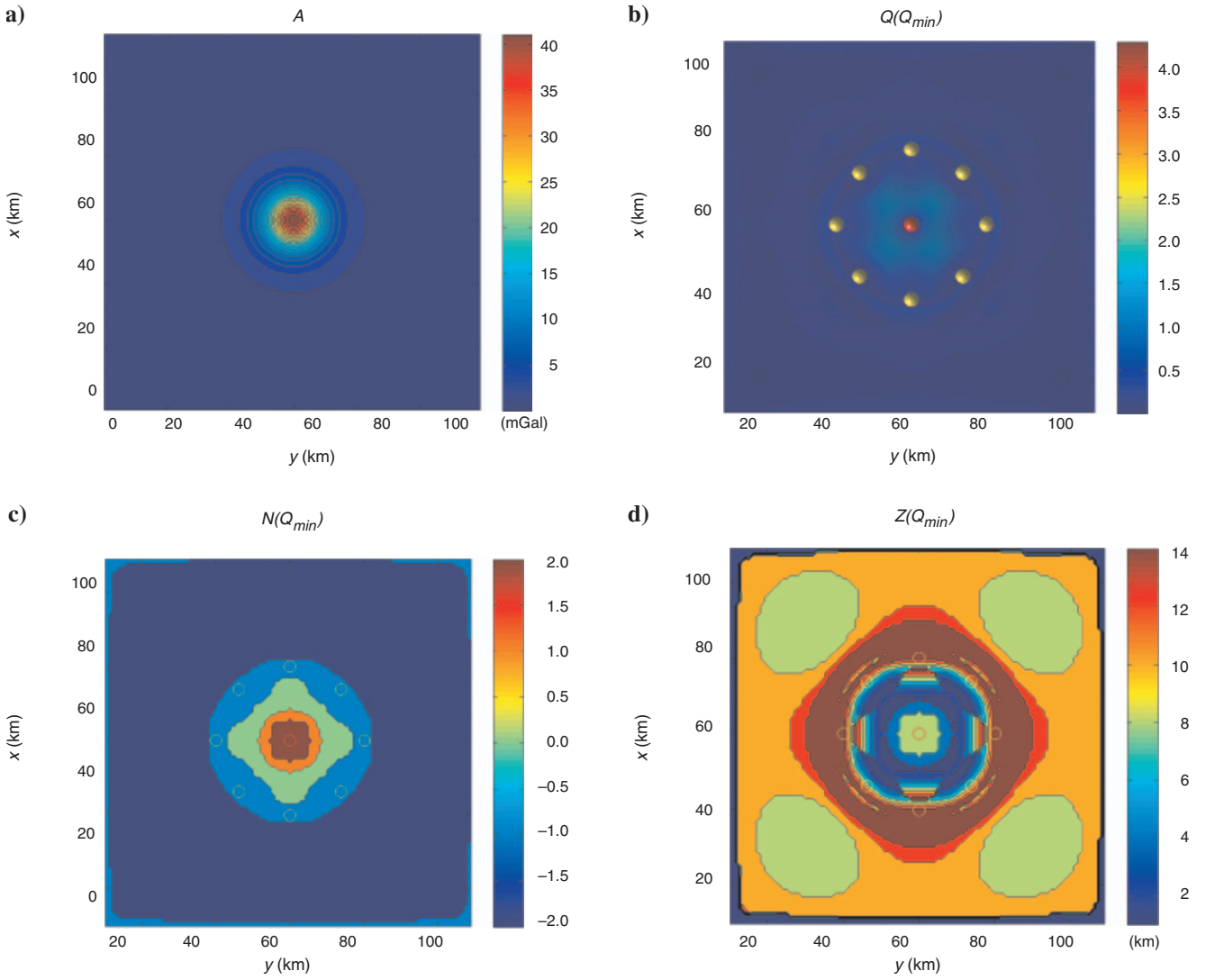

Figure 6. Model gravity data set caused by a sphere (point mass) and MaGSoundDST results: (a) gravity field, mGal; (b) $Q(Q_{\min})$; (c) $N(Q_{\min})$; (d) $Z(Q_{\min})$ km. The accepted minima of $Q(Q_{\min})$ for $q_A > (q_A)_{\min} = 165$ mGal, which is 75% of the maximum of q_A, are marked with red circles. The rejected ones are marked with yellow circles.

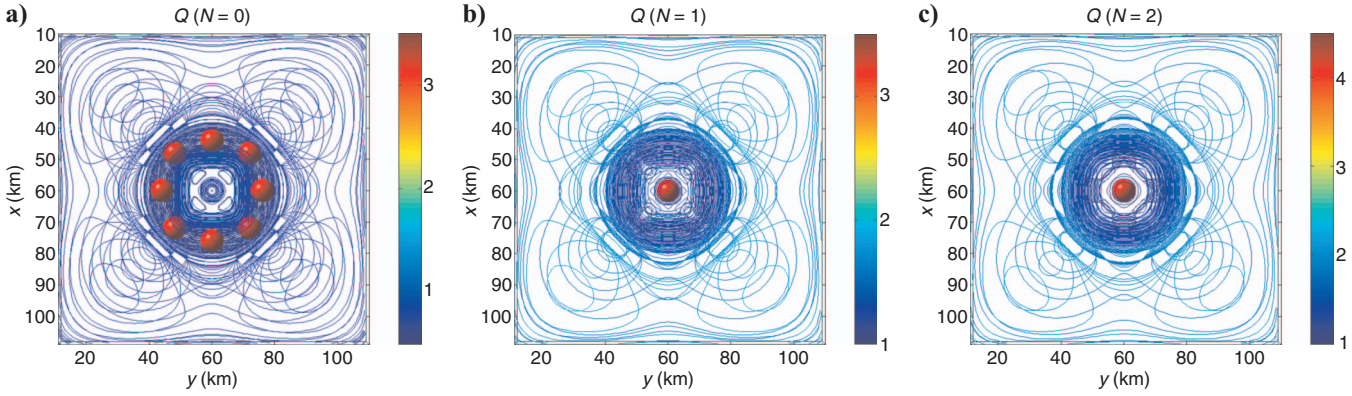

Figure 7. The 3D maps of the estimator $Q(a,b,c;N)$ of the DST for the case of a sphere (point mass) for structural indices $N = 0$, 1, and 2. The red spheres denote the location of local minima of $Q(a,b,c;N)$ and thus of singular points of sources. The view of the 3D contour maps Q has an azimuth of zero and elevation of $-90°$.

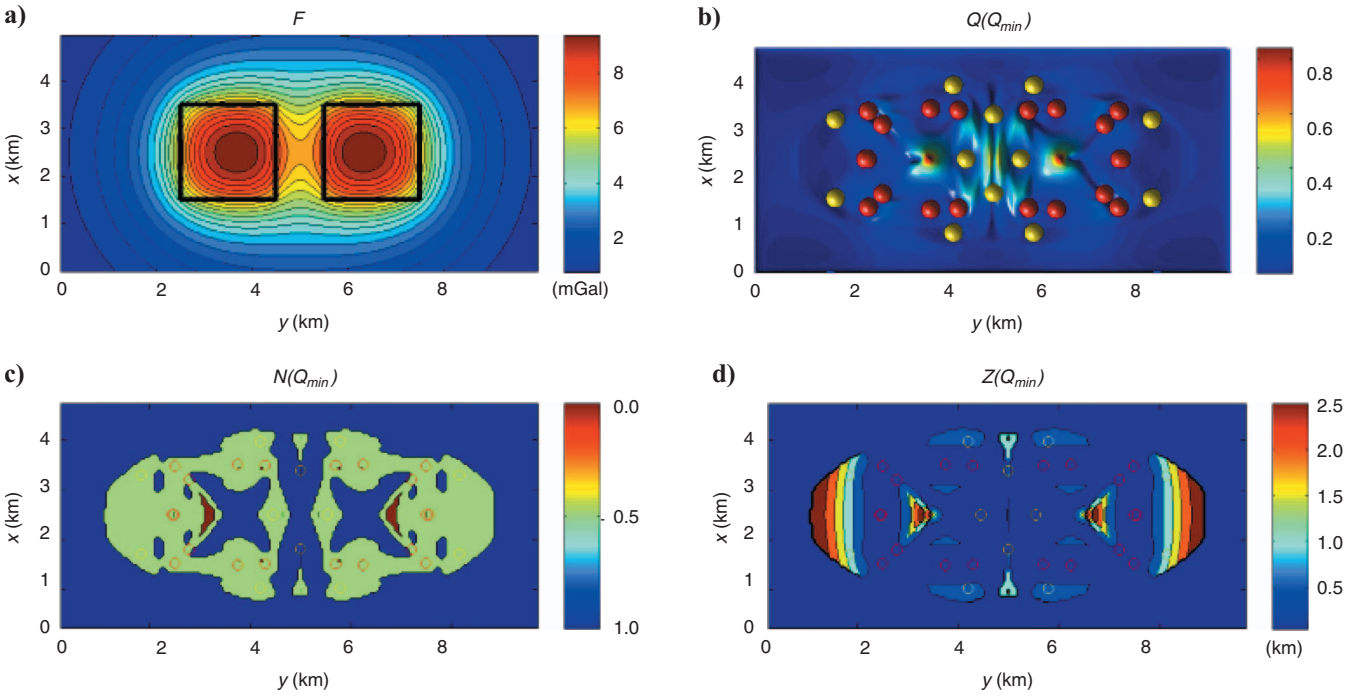

Figure 8. Model gravity data set caused by two vertical prisms and MaGSoundDST results: (a) gravity field, mGal; (b) $Q(Q_{\min})$; (c) $N(Q_{\min})$; (d) $Z(Q_{\min})$ km. The accepted minima of $Q(Q_{\min})$ for $q_F > (q_F)_{\min} = 7.5$ mGal are marked with red circles. The rejected ones are marked with yellow circles.

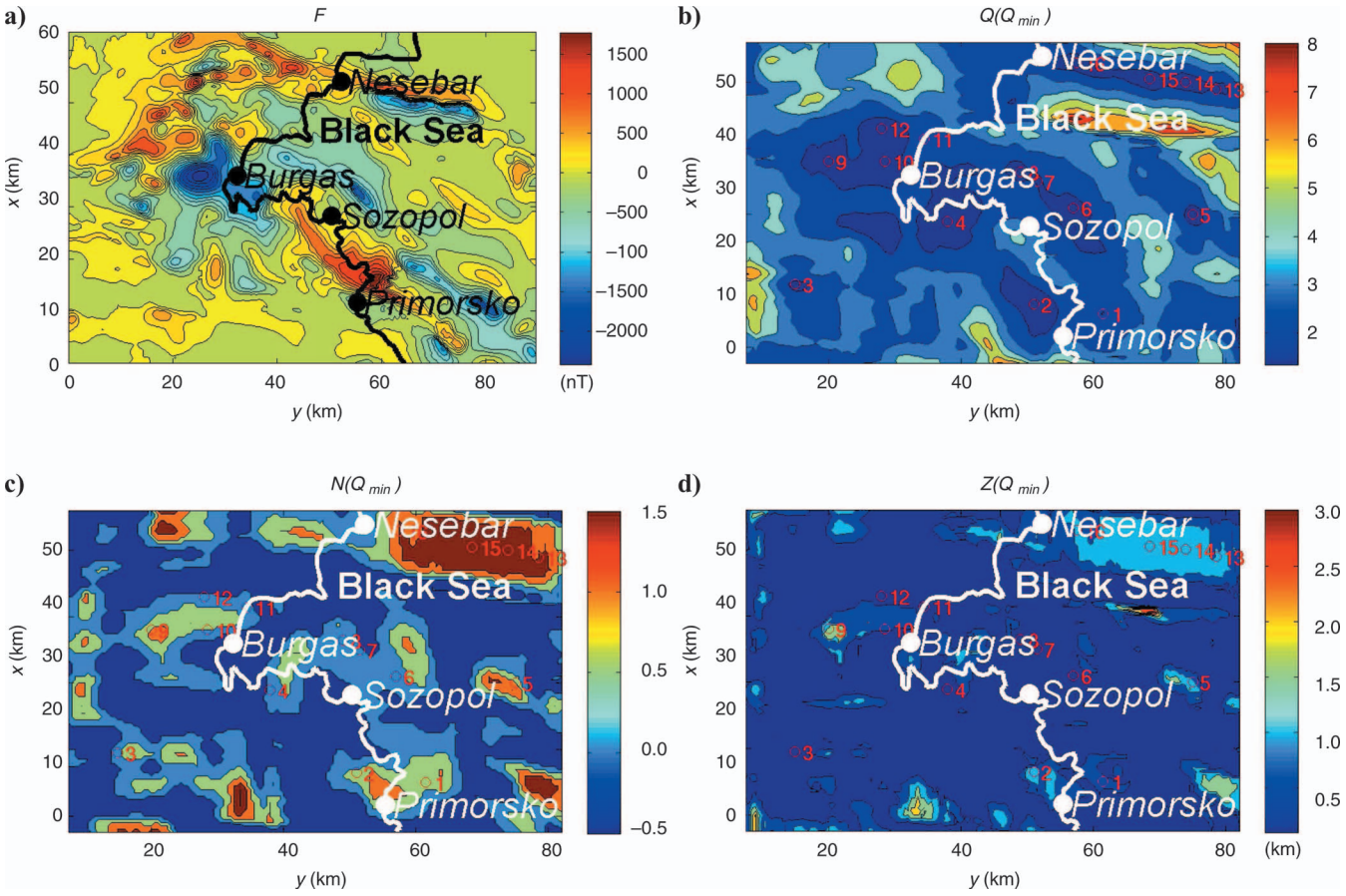

Figure 9. Field data from the Burgas region and the adjoining Black sea shelf and MaGSoundDST results: (a) anomalous magnetic field ΔT, in nT; (b) $Q(Q_{\min})$; (c) $N(Q_{\min})$; (d) $Z(Q_{\min})$ km.

Table 2. Estimated parameters (a km, b km, c km, N_{est}) of magnetic field sources in the Burgas region of southeast Bulgaria and the adjoining Black Sea shelf.

Number	N_{est}	a	b	c	$(Q(Q_{min}))_{min}$
1	0.5	15.1	61.5	0.5	1.99
2	0.5	16.5	51.2	1.2	1.41
3	0.0	19.4	15.2	0.2	1.73
4	0.0	29.2	38.1	0.2	1.38
5	1.0	29.9	75.2	1.3	1.66
6	0.0	30.9	56.9	0.1	1.63
7	0.0	35.9	51.1	0.2	1.89
8	0.0	36.8	48.8	0.3	1.68
9	1.0	38.0	20.0	1.9	1.56
10	0.5	38.1	28.3	0.7	1.53
11	0.0	41.5	34.5	0.2	1.98
12	0.0	42.8	28.2	0.1	1.40
13	1.5	49.2	78.6	1.1	1.79
14	1.5	50.2	73.7	1.0	1.58
15	1.5	50.3	68.7	1.2	1.42
16	1.5	52.9	57.7	1.3	1.64

CONCLUSION

MaGSoundDST belongs to the same group of inversion procedures as the popular Euler deconvolution method, based on the homogeneity property of the anomaly fields of simple gravity and magnetic sources. In contrast to all variations of the Euler deconvolution method, which use a moving window, MaGSoundDST gives a single solution corresponding to each detected simple source. Conversely, all Euler deconvolution techniques give numerous spurious solutions, corresponding to a single simple source, posing the need for clustering techniques to refer these many solutions to their corresponding sources. The simplicity of the output of the MaGSoundDST procedure is its major advantage over all Euler deconvolution procedures. In spite of the use of a moving window, with MaGSoundDST we achieved fewer solutions, compared to the Euler deconvolution method. This means it is even feasible for the interpreter to check the solutions manually.

An additional advantage of MaGSoundDST over the conventional Euler deconvolution technique is that it takes into account a linear background, whereas the latter limits itself to accounting for only a constant background; hence, MaGSoundDST is less susceptible to interference from nearby sources. MaGSoundDST is an important alternative approach for automatic, magnetic, and gravity data inversion, combining a global moving-window method wherein each solution links to singular points of causative bodies and where, through the compilation of three new maps, $Q(Q_{min})$, $N(Q_{min})$ and $Z(Q_{min})$, the solutions link to real sources.

MaGSoundDST is a new methodology applicable to any class of optimization problems for which there is no more than one solution in a projected space. Thus, the approach is applicable to a broad class of inversion problems, including those related by Euler's equation. In this sense, it is possible to apply the approach directly to Euler's equation at the center of the window and choose the solution based on the misfit for different values of depth and structural indices. However, accounting for a linear background field in this case makes the problem nonlinear.

ACKNOWLEDGMENTS

We are grateful to the reviewer, Afif Saad; Associate Editor Xiong Li; and three anonymous reviewers for their helpful comments. This work was funded by the Natural Research Council (U.K.) grant NER/0/S/2003/00674.

APPENDIX A

DERIVATION OF THE ANALYTICAL EXPRESSION OF THE DST FROM THE EXPRESSION FOR THE FDST

Expression 3 for the FDST leads to expression 4 for the DST as the limit of D when t tends to 1:

$$S(P) = \lim_{t\to 1} D(P') = \lim_{t\to 1} \frac{A'(P') - A(P')}{t-1} \text{ when } P' \to P. \tag{A-1}$$

The latter leads to $A'(P')\to A(P)$ and $A(P')\to A(P)$, i.e., $A'(P') - A(P')\to 0$ when $t\to 1$.

The $0/0$ uncertainty when $t\to 1$ can be resolved using l'Hospital's rule:

$$S(P) = \lim_{t\to 1} \frac{\partial[A'(P') - A(P')]/\partial t}{\partial(t-1)/\partial t}, \tag{A-2}$$

where $A'(P') = t^n A(P)$ is the transform of similarity of $A(x,y,z)$ to $A'(x',y',z')$ from point $C(a,b,c)$. Thus, because

$$\frac{\partial A'(P')}{\partial t} = \frac{\partial t^n A(P)}{\partial t} = nt^{n-1}A(P) \text{ and}$$

$$\frac{\partial A(P')}{\partial t} = \frac{\partial A(P')}{\partial x}\frac{\partial x'}{\partial t} + \frac{\partial A(P')}{\partial y}\frac{\partial y'}{\partial t} + \frac{\partial A(P')}{\partial z}\frac{\partial z'}{\partial t},$$

and according to equation 1

$$\frac{\partial x'}{\partial t} = x - a, \quad \frac{\partial y'}{\partial t} = y - b, \quad \frac{\partial z'}{\partial t} = z - c,$$

$$\frac{\partial(t-1)}{\partial t} = 1,$$

then

$$\lim_{t\to 1} D(x',y',z') = nA(x,y,z) + (a-x)\frac{\partial A}{\partial x} + (b-y)\frac{\partial A}{\partial y} + (c-z)\frac{\partial A}{\partial z} = S(x,y,z), \tag{A-3}$$

which is equal to equation 4 for the DST.

APPENDIX B

EXPRESSION FOR THE DST GENERATED FROM THE GRAVITY POTENTIAL OF A POINT MASS

The gravity potential V of a point mass m has the well-known expression $V(x,y,z) = Gm/r_{MP}$, where G is the gravitational constant, $r_{MP} = ((x-x_0)^2 + (y-y_0)^2 + (z-z_0)^2)^{1/2}$ is the distance between the mass m at point $M(x_0,y_0,z_0)$ and the observation point $P(x,y,z)$. The degree of Euler homogeneity of V is $n = -1$. Then, according to the DST equation 4,

$$S_V(x,y,z) = -\frac{Gm}{r_{MP}} + Gm\left((a-x)\frac{\partial}{\partial x}\left(\frac{1}{r_{MP}}\right) + (b-y)\frac{\partial}{\partial y}\left(\frac{1}{r_{MP}}\right) + (c-z)\frac{\partial}{\partial z}\left(\frac{1}{r_{MP}}\right)\right). \quad \text{(B-1)}$$

Substituting equations

$$a - x = (a - x_0) + (x_0 - x), \quad b - y = (b - y_0) + (y_0 - y), \quad c - z = (c - z_0) + (z_0 - z),$$

$$\frac{\partial}{\partial x}\left(\frac{1}{r_{MP}}\right) = \frac{x_0 - x}{{r_{MP}}^3}, \quad \frac{\partial}{\partial x}\left(\frac{1}{r_{MP}}\right) = \frac{y_0 - y}{{r_{MP}}^3},$$

and

$$\frac{\partial}{\partial z}\left(\frac{1}{r_{MP}}\right) = \frac{z_0 - z}{{r_{MP}}^3}$$

into equation B-1 and after simple manipulations, taking into account $\nabla_P V = -\nabla_M V$, we obtain

$$S_V(x,y,z) = -\frac{Gm}{r_{MP}} + Gm\left((x_0-a)\frac{\partial}{\partial x}\left(\frac{1}{r_{MP}}\right) + (y_0-b)\frac{\partial}{\partial y}\left(\frac{1}{r_{MP}}\right) + (z_0-c)\frac{\partial}{\partial z}\left(\frac{1}{r_{MP}}\right)\right) + \frac{Gm}{r_{MP}}, \quad \text{(B-2)}$$

where the sum of the first and third term is zero and the second term is the analytical expression for the potential U created by a point dipole at point $M(x_0,y_0,z_0)$ with a moment $Gm\mathbf{r}_{CM}$ proportional to the distance r_{CM} and the mass m. This is a gravity dipole as an equivalent source of the DST field $S_V(x,y,z)$ (Stavrev, 1997).

REFERENCES

Dachev, H., 1988, Structure of the earth's crust in Bulgaria: Technika (in Bulgarian).

Dewangan, P., T. Ramprasad, M. V. Ramana, M. Desa, and B. Shailaja, 2007, Automatic interpretation of magnetic data using Euler deconvolution with nonlinear background: Pure and Applied Geophysics, **164**, 2359–2372.

Fedi, M., 2007, DEXP: A fast method to determine the depth and the structural index of potential field sources: Geophysics, **72**, no. 1, I1–I11.

Gellert, W., H. Kastner, and S. Neuber, 1979, Lexikon der Mathematik: VEB Bibliographisches Institut (in German).

Gerovska, D., and M. J. Araúzo-Bravo, 2003, Automatic interpretation of magnetic data based on Euler deconvolution with unprescribed structural index: Computers & Geosciences, **29**, 949–960.

Gerovska, D., M. J. Araúzo-Bravo, and P. Stavrev, 2009, Estimating the magnetization direction of sources from southeast Bulgaria through correlation between reduced-to-the-pole and total magnitude anomalies: Geophysical Prospecting, **57**, 491–505.

Gerovska, D., P. Stavrev, and M. J. Araúzo-Bravo, 2005, Finite-difference Euler deconvolution algorithm applied to the interpretation of magnetic data from northern Bulgaria: Pure and Applied Geophysics, **162**, 591–608.

Hansen, R. O., and M. Simmonds, 1993, Multiple source Werner deconvolution: Geophysics, **58**, 1792–1800.

Hartman, R., B. J. Teskey, and J. L. Friedberg, 1971, A system for rapid digital aeromagnetic interpretation: Geophysics, **36**, 891–918.

Hsu, S. K., 2002, Imaging magnetic sources using Euler's equation: Geophysical Prospecting, **50**, 15–25.

Keating, P. B., 1998, Weighted Euler deconvolution of gravity data: Geophysics, **63**, 1595–1603.

Keating, P., and M. Pilkington, 2004, Euler deconvolution of the analytic signal and its application to magnetic interpretation: Geophysical Prospecting, **52**, 165–182.

Mikhailov, V., A. Galdeano, M. Diament, A. Gvishiani, S. Agayan, S. Bogoutdinov, E. Graeva, and P. Sailhac, 2003, Application of artificial intelligence for Euler solutions clustering: Geophysics, **68**, 168–180.

Moreau, F., D. Gilbert, M. Holschneider, and G. Saracco, 1997, Wavelet analysis of potential fields: Inverse Problems, **13**, 165–178.

Nabighian, M. N., V. J. S. Grauch, R. O. Hansen, T. R. LaFehr, Y. Li, J. W. Peirce, J. D. Phillips, and M. E. Ruder, 2005, The historical development of the magnetic method in exploration: Geophysics, **70**, no. 6, ND22–ND61.

Naudy, H., 1971, Automatic determination of depth on aeromagnetic profiles: Geophysics, **36**, 717–722.

Reid, A. B., J. M. Allsop, H. Granser, A. J. Millet, and I. W. Somerton, 1990, Magnetic interpretation in three dimensions using Euler deconvolution: Geophysics, **55**, 80–91.

Sheriff, R. E., 2002, Encyclopedic dictionary of applied geophysics: SEG.

Stavrev, P., 1997, Euler deconvolution using differential similarity transformations of gravity or magnetic anomalies: Geophysical Prospecting, **45**, 207–246.

———, 2006, Inversion of elongated magnetic anomalies using magnitude transforms: Geophysical Prospecting, **54**, 153–166.

Stavrev, P., and D. Gerovska, 2000, Magnetic field transforms with low sensitivity to the direction of source magnetization and high centricity: Geophysical Prospecting, **48**, 317–340.

Stavrev, P., D. Gerovska, and M. J. Araúzo-Bravo, 2006, Automatic inversion of magnetic anomalies from two height levels using finite-difference similarity transforms: Geophysics, **71**, no. 6, L75–L86.

———, 2009, Depth and shape estimates from simultaneous inversion of magnetic fields and their gradient components using differential similarity transforms: Geophysical Prospecting, **57**, 707–717.

Stavrev, P., and A. Reid, 2007, Degrees of homogeneity of potential fields and structural indices of Euler deconvolution: Geophysics, **72**, no. 1, L1–L12.

Thompson, D. T., 1982, EULDPH: A new technique for making computer-assisted depth estimates from magnetic data: Geophysics, **47**, 31–37.

Thurston, J. B., and R. S. Smith, 1997, Automatic conversion of magnetic data to depth, dip, and susceptibility contrast using the SPI™ method: Geophysics, **62**, 807–813.

Ugalde, H., and B. Morris, 2008, Cluster analysis of Euler deconvolution solutions: New filtering techniques and actual link to geological structure: 78th Annual International Meeting, SEG, Expanded Abstracts, 794–798.